Motor-Temperature-Aware Optimal Energy Management for Dual-Motor Electric Buses

Sheng Yu, Cuneyt Haspolat, Yaprak Yalcin, Saleh Msaddi, Boli Chen, Simos A. Evangelou and Imad M. Jaimoukha

***Abstract*— This work studies the energy management performance of heavy-duty electric buses (EBs) equipped with two electric motors onboard their powertrains. Instead of merely considering the effects of load torque and angular speed on motor efficiency, the proposed optimal scheme further includes the effect of different temperatures on motor performance. After identifying a novel motor temperature model and generating temperature-dependent three-dimensional motor efficiency maps based on experimentally collected data, the energy management task is formulated as an optimal control problem and solved by dynamic programming that guarantees the global optimality of the generated solution. Compared with an existing single-motor powertrain and dual-motor powertrain controlled by benchmark strategies, the heavy-duty EB can benefit from a maximum of 11.96% battery electric energy consumption saving after utilizing the proposed temperature-aware optimal dual-motor energy management scheme.**

I. INTRODUCTION

As the number of electric vehicles has increased worldwide in recent years [1], the decarbonization of road transportation which accounts for a large amount of greenhouse gas emissions has achieved significant progress. Thanks to the development of electric motor, power battery, and electronic control system technologies of the new energy vehicles, an increasing number of battery electric vehicles (BEVs) have adopted two motors in their powertrains to enhance performance, efficiency, and adaptability [2]. Unlike single-motor vehicles, dual-motor BEVs leverage the advantages of distributing power between both electric motors by considering dual-motor powertrain topologies such as single-axle driven [3] and distributed driven [4], [5] topologies. This arrangement enables more precise control over power delivery and torque distribution, resulting in improved acceleration, handling, and overall vehicle performance. Furthermore, since electric motor energy conversion efficiency varies significantly as its operation region changes, with two motors available, the power distribution scheme has a degree of freedom to allocate the operating points of both motors at more efficient operating regions to save energy consumption, while satisfying the overall driving demand [6], [7]. In dual-motor BEVs, employing optimization-based control techniques such as dynamic programming (DP) [8], [9] and rule-based control schemes [10] can enable motors to be adaptively operated to changing environments, achieving precise torque distribution and efficient energy management in dual-motor BEVs [11].

In addition to output load torque and angular speed, electric motor energy conversion efficiency is also tightly dependent on its working temperature. Elevated temperatures can significantly influence the performance of motor operation. Keeping motors continuously working at improper thermal conditions can negatively affect the core, insulation, and permanent magnets, thus reducing the machine's performance and life span [12]. For example, when the motor temperature rises excessively, the overheated motor may face insulation failure of the stator winding [13]. The rotor magnets can also become irreversibly demagnetized, which might stop the machine from functioning properly [14]. Moreover, different temperatures correlate to copper and iron losses during energy conversion [15]. Thus, it is important to operate motors at proper temperature ranges to maintain higher energy conversion efficiencies for the best energy economy.

Other than small-size passenger vehicles, the electrification of heavy-duty vehicles, such as public buses, has also attracted attention from academics, automotive industry, and governments [16], [17], [18], [19]. However, since heavy-duty electric buses (EBs) require more powerful and efficient driving systems than light-duty vehicles due to their special weight specifications and range requirements, their electrification is more complicated and challenging [20], [21]. Although some manufacturers have released electrified double-deck buses such as Enviro400EV [22] and VolvoBZL electric [23] for London public bus service operators, the permitted gross vehicle weights (GVWs) of these types are usually below 20 tons and are designed particularly for urban public bus services. There is still a need to investigate heavy-duty double-deck buses for long-distance intercity travel that are over 20 tons [24], [25].

To address this gap, this work proposes an electrification solution for heavy-duty intercity buses by equipping their powertrain with dual motors and designing a novel motor-temperature-aware optimal electric energy management scheme. The detailed contribution of the paper is threefold: 1) identification of the realistic electric motor temperature dynamics and generation of motor energy conversion efficiency maps at different temperatures based on experimentally collected data; 2) formulation of a novel temperature-aware optimal control problem (designated as OCP-T) aiming to minimize the overall energy consumption of a dual-motor EB; 3) investigation of the performance of the proposed OCP-T method which is shown to outperform the energy consumption of existing benchmarks with either a different powertrain architecture (single-motor electric powertrain) or same powertrain architecture with different power distribution strategies of a typical heavy-duty three-axle double-deck EB model.

The rest of the paper begins in Section II with an introduction to the model identification, followed by Section III which formulates the optimal control problem. Moreover, simulation results and comparisons are illustrated and evaluated in Section IV. Finally, conclusions are provided and a future work plan is suggested in Section V.

S. Yu, S. A. Evangelou, and I. M. Jaimoukha are with the Dept. of Electrical and Electronic Engineering at Imperial College London, UK (sheng.yu17@imperial.ac.uk, s.evangelou@imperial.ac.uk, i.jaimouka@imperial.ac.uk)

C. Haspolat and S. Msaddi are at AVL Türkiye Research & Engineering, Istanbul, Türkiye (cuneyt.haspolat@avl.com, saleh.msaddi@avl.com)

Y. Yalcin is with the Dept. of Control and Automation Engineering at Istanbul Technical University, Türkiye (yalciny@itu.edu.tr)

B. Chen is with the Dept. of Electronic and Electrical Engineering at University College London, UK (boli.chen@ucl.ac.uk)

II. Motor Temperature Model Identification

This work focuses on a heavy-duty EB powertrain that is equipped with two identical motors and associated electric cooling pumps, as illustrated in Fig. 1. The battery provides electric energy for both permanent magnet synchronous (PMS) motors that deliver mechanical torques in parallel to drive or regeneratively brake the bus through the transmission. Electrical and mechanical power flows within the powertrain are represented by green and blue arrows, respectively, in Fig. 1. The motor temperature (refers to the rotor temperature in this paper) increases when a motor is in use. The associated cooling system (pump) is triggered once the motor reaches a threshold temperature. Then, the cooling pump draws constant power from the same battery and cools down the motor. Purple arrows represent work done by cooling systems towards associated motors to reduce temperatures.

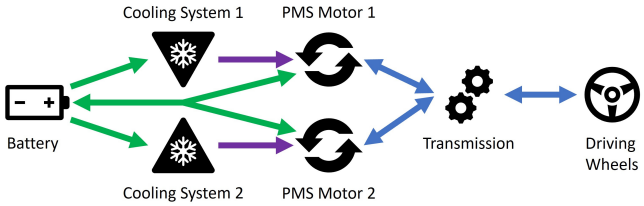

Fig. 1: Block diagram of the EB powertrain with two identical PMS motors and coupled cooling systems.

To identify the motor temperature model, data of motor temperature corresponding to motor input power and pump power are experimentally collected by operating the powertrain testbed subject to the WLTP drive cycle for one hour, with a sampling interval of 0.01 s. The investigated motor is a VOITH motor [26] that has been used in real-world buses. The collected data on motor temperature can be precisely fitted by a continuous-time first-order system that includes two inputs (motor input electric power $P_{e,i}$ and cooling pump power P_p) and one output (the derivative of the temperature difference between the motor and the ambient, $\Delta T_i = T_i - T_{amb}$) as illustrated in Fig. 2, where T_i is the temperature of Motor i and T_{amb} is the ambient temperature. The subscript $i \in \{1,2\}$ is the motor index (indicating Motor 1 or Motor 2). The input power $P_{e,i}$ is determined by the motor output torque, angular speed, and energy conversion efficiency (see (3) below). The cooling pump power P_p is a constant parameter. Moreover, $S_i \in \{0,1\}$ is the switch status of the cooling pump. $S_i = 0$ indicates Pump i is off and no electric energy is consumed and $S_i = 1$ means Pump i is on and consumes the battery energy at a power of P_p. The cooling pumps are triggered automatically once the temperature of the associated motor T_i reaches the predefined and fixed threshold (65°C) and turn off when the temperature drops below the threshold. The transfer functions of blocks G_1 and G_2 are obtained by MATLAB System Identification Toolbox with a zero initial condition (motor temperature is the same as ambient).

After discretization, the identified discrete-time model is

$$\Delta T_i(k+1) = \Delta T_i(k) + (-a\Delta T_i(k) + k_1|P_{e,i}(k)| + k_2 S_i(k) P_p)\delta t, \quad (1)$$

where $a = 6.05 \times 10^{-4}\,\mathrm{s}^{-1}$, $k_1 = 8.7 \times 10^{-7}\,\frac{^\circ\mathrm{C}}{\mathrm{J}}$, and $k_2 = -1.46 \times 10^{-5}\,\frac{^\circ\mathrm{C}}{\mathrm{J}}$ are fitting parameters of the model, with the coefficient of determination, $R^2 = 0.9945$. The sampling index $k \in \mathbb{N}_{[0,\bar{k}]}$ with the total number of samples $\bar{k} = T_f/\delta t \in \mathbb{N}_{>0}$ (T_f is the predefined total time of the driving cycle). $\delta t \in \mathbb{R}_{>0}$ is the sampling interval. The cooling pump switch $S_i(k)$ is passively controlled by the motor temperature as

$$S_i(k) = \begin{cases} 1, & \forall\ T_i(k) \geq 65^\circ\mathrm{C}, \\ 0, & \forall\ T_i(k) < 65^\circ\mathrm{C}. \end{cases} \quad (2)$$

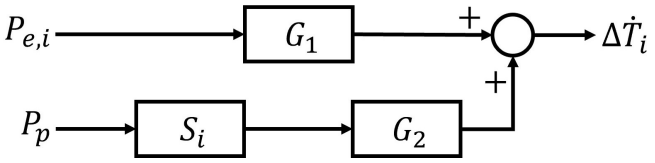

Fig. 2: Block diagram of motor temperature model for Motor i, where $i \in \{1,2\}$ represents the motor index.

To further monitor the relationship between motor input electric power and output torque and angular speed at different temperatures, realistic motor energy conversion efficiencies are experimentally collected as the motor temperature increases from 25°C to 70°C in steps of 5°C at various torque-speed operating points, ranging from 200 Nm to 3000 Nm torques in steps of 200 Nm, and 200 rpm to 3800 rpm angular speeds in steps of 200 rpm (operating points outside the motor output power limits of ±310 kW are excluded). Motor energy conversion efficiency maps used in the present work are produced by numerical interpolation of the experimentally collected efficiencies in order to provide finer grids, while some efficiency data at corner operating points, for example at torques below 200 Nm or operating points close to the power limits, are obtained by numerical extrapolation. Fig. 3a shows motor efficiency maps at temperatures of 25°C, 45°C, and 65°C (due to space constraints, only three representative maps are presented). Moreover, the motor efficiency variation with temperature for two typical operating point examples with the same angular speed (1000 rpm) is shown in Fig. 3b. When the temperature increases from 25°C to 65°C, the energy conversion efficiency of the 600 Nm torque operating point reduces by 2.95%, from 94.9% to 92.1%. Meanwhile, the efficiency of another operating point with the same angular speed but a larger torque magnitude at 1000 Nm decreases by less than 1%, from 95.4% to 93.5% . The efficiency maps and profiles illustrate that, fixing the angular speed and torque, the energy conversion efficiency decreases as the temperature increases. Moreover, the efficiencies at small-magnitude torques are more sensitive to temperature changes compared to those at large-magnitude torques.

III. Optimal Control Problem Formulation

The electrical power of the Motor i, $P_{e,i}(k)$ in (1) can be further determined by

$$P_{e,i}(k) = \frac{P_{m,i}(k)}{\eta_i(\tau_i(k), \omega(k), T_i(k))^{\mathrm{sign}(\tau_i(k))}}, \quad (3)$$

where $P_{m,i}(k) = \tau_i(k)\omega(k)$ represents the mechanical output power of Motor i. $\tau_i(k)$ is the output load torque of Motor i and $\omega(k)$ is the motor angular speed (identical for both motors) which is further determined by the bus speed. $\eta_i(\tau_i(k), \omega(k), T_i(k))^{\mathrm{sign}(\tau_i(k))}$ is the energy conversion efficiency factor of Motor i. It is noticeable that, in addition to the torque and angular speed, the energy conversion efficiency factor in this work is further dependent on the temperature of the PMS machine, leading to a three-dimensional efficiency factor map as illustrated in Fig. 3a.

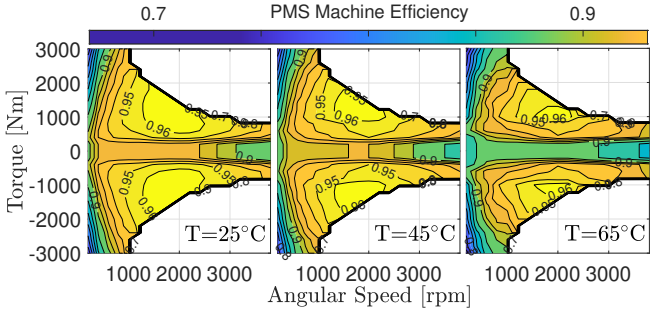

(a) Experimentally collected energy conversion efficiency maps of the studied PMS machine (model: VOITH Liquid-cooled IPSM HD e-motor [26]) at different temperatures.

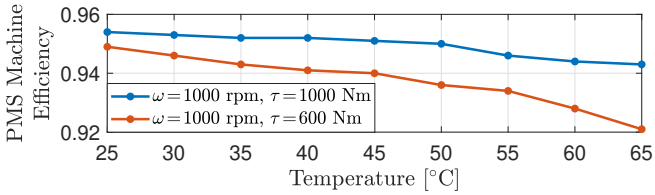

(b) Efficiency profiles of PMS machine at two operating points.

Fig. 3: Maps and profiles of PMS machine efficiency with respect to temperature.

Therefore, the efficiency factor $\eta_i(k)$ is jointly determined by $\tau_i(k)$, $\omega(k)$, and $T_i(k)$ in the proposed control scheme when optimizing the performance. The EB studied in this paper is equipped with two identical PMS motors, hence they share the identical temperature dynamic model as shown in (1) and the efficiency map in Fig. 3a.

In addition to the temperature dynamic equations (1), the vehicle powertrain is physically limited by the following motor inequality constraints

$$\underline{P_m} \le P_{m,i}(k) \le \overline{P}_m, \tag{4a}$$
$$\underline{T} \le T_i(k) \le \overline{T}, \tag{4b}$$
$$\underline{\tau} \le \tau_i(k) \le \overline{\tau}, \tag{4c}$$

where $\underline{P_m}$ and $\overline{P}_m$, $\underline{T}$ and $\overline{T}$, and $\underline{\tau}$ and $\overline{\tau}$ are the minimum and maximum motor output power, operating temperatures, and output load torques, respectively. Furthermore, the total output torque of the two motors should meet the predefined demanded driving torque of the EB, $\tau_d(k)$, as

$$\tau_d(k) = \tau_1(k) + \tau_2(k), \tag{5}$$

where $\tau_d(k)$ is determined by the EB overall demanded output mechanical power ($P_m(k)$) and motor speed ($\omega(k)$)

$$\tau_d(k) = \frac{P_m(k)}{\omega(k)}, \quad \forall \omega(k) \neq 0, \tag{6a}$$
$$P_m(k) = (ma(k) + 0.5\rho A f_d v(k)^2 + mgf_r)v(k). \tag{6b}$$

$P_m(k)$ is the sum of output mechanical power from two motors, i.e., $P_m(k) = P_{m,1}(k) + P_{m,2}(k)$, describing the power required to follow the specified driving cycle while overcoming losses including the air-drag and tire-rolling resistances. m is the EB mass, $v(k)$ and $a(k)$ are the EB velocity and acceleration, respectively (determined from the drive cycle). g is the gravitational field strength, ρ is the air density, A is the EB front sectional area, and f_d and f_r are coefficients of air-drag and tire-rolling, respectively.

Since the optimization aims to minimize the overall battery energy consumption which is the energy source of both motors and pumps, the objective function is designed as the sum of the energy consumption by all motors and pumps for the whole drive cycle, as $V = \sum_{k=0}^{\bar{k}} J(k)\delta t$, where

$$J(k) = (P_{e,1}(k) + S_1(k)P_p) + (P_{e,2}(k) + S_2(k)P_p). \tag{7}$$

Therefore, the temperature-aware optimal control problem considering thermal effects on motor efficiencies (designated as OCP-T) can be summarized as

$$\min_{\boldsymbol{\tau_1}} \quad V = \sum_{k=0}^{\bar{k}} J(k)\delta t\,, \tag{8a}$$
$$\textbf{s. t.:} \quad (1),(2),(3),(4),(5),(6),(7), \quad k = 0,1,2,\ldots,\bar{k}, \tag{8b}$$
$$\textbf{given:} \quad T_1(0) = T_2(0) = T_{amb}. \tag{8c}$$

where $\boldsymbol{\tau_1} = [\tau_1(0), \tau_1(1), \ldots, \tau_1(\bar{k})]$, the vector of Motor 1 output torques $\tau_1(k)$, is the control variable, and $\tau_d(k)$ as well as $\omega(k)$ are exogenous inputs predetermined from the chosen drive cycle.

IV. Numerical Results

This section demonstrates and evaluates the performances of the EB powertrain after solving the OCP-T in (8). The presented results are twofold: 1) a performance evaluation of the proposed temperature-aware optimal dual-motor powertrain control method (OCP-T) that utilizes the temperature-dependent energy conversion efficiency maps; 2) a comparison of the energy consumption performances of the proposed OCP-T with other existing benchmarks including a single-motor powertrain benchmark, two rule-based dual-motor powertrain benchmarks, and an optimization-based dual-motor powertrain benchmark but utilizing the temperature-unaware efficiency map at the ambient temperature (designated as OCP-A). Both OCPs (OCP-T and OCP-A) in this work are solved by the identical dynamic programming (DP) solver to guarantee the global optimality of the solutions [27]. The energy consumption results of all methods are calculated according to the realistic efficiency maps in Fig. 3a, with more explanations given later in Table II. The main characteristic parameters of the simulation are summarized in Table. I. The parameters of the double-deck bus are derived from a VOLVO BZR Low Entry Electric 6×2 double-deck chassis [25]. The specifications of the electric motors as well as corresponding cooling pumps adopted in this work for both single- and dual-motor powertrains are identical, according to the VOITH HD e-motor [26]. The mass difference caused by different numbers of motors is neglected while keeping the overall mass of the EB consistent for all tested methods. To accurately assess the energy consumption performance in real-world driving conditions, the EB is assumed to drive the UK Bus Cycle (UKBC) [28] as shown by Fig. 4, for two consecutive test iterations as the simulated driving mission. The initial temperatures of both motors are at the ambient temperature. The sampling interval of the controller is set to $\delta t = 1$ s.

A. Temperature-aware OCP (OCP-T) performances

This subsection presents the performances of the proposed OCP-T dual-motor control method. Fig. 5 records profiles of the temperature and cooling pump status of each motor. The temperatures of both motors increase from the beginning as both are activated. Nevertheless, the temperature of Motor 1 is higher than the temperature of Motor 2 during the mission, which makes the original identical motors have

TABLE I: Parameters of double-deck EB, motor, and pump.

Description	Symbol	Value
Ambient temperature	T_{amb}	25°C
Air density at ambient temperature	ρ	1.184 kg/m^3
Air-drag coefficient	f_d	0.6
Tire-rolling resistance coefficient	f_t	0.01
EB mass	m	25000 kg
EB frontal sectional area	A	10 m^2
EB final gear ratio		7.36
EB wheel radius		0.50625 m
Motor minimum/maximum output power	$\underline{P}_m/\overline{P}_m$	-310/310 kW
Motor lowest/highest operating temperature	$\underline{T}/\overline{T}$	-30/125 °C
Motor minimum/maximum torque	$\underline{\tau}/\overline{\tau}$	-3100/3100 Nm
Motor maximum angular speed		3800 rpm
Pump working power	P_p	160 W

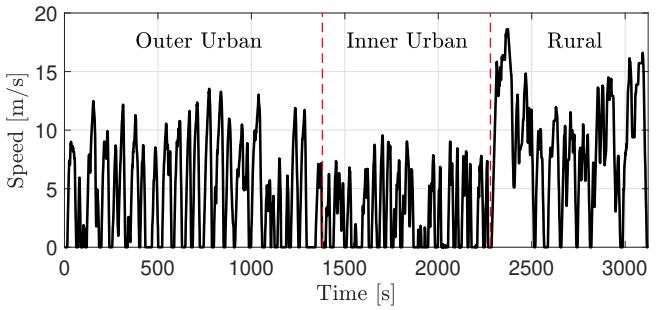

Fig. 4: The velocity profile of the UK Bus Cycle (UKBC), which consists of three consecutive phases in outer urban, inner urban, and rural areas, respectively.

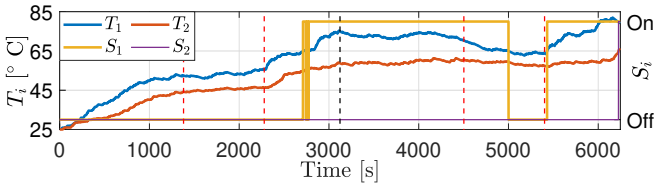

Fig. 5: Profiles of T_1, S_1 of Motor 1 and T_2, S_2 of Motor 2 for two consecutive UKBC iterations. Red and black vertical dashed lines separate phases within each UKBC iteration and the two UKBC iterations, respectively.

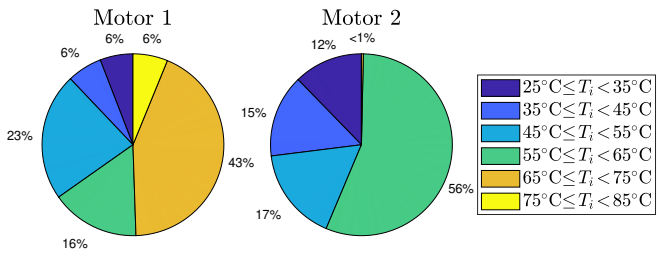

Fig. 6: Pie charts of motor temperature duration as percentages of the mission total time, from the perspective of Motor 1 and Motor 2, respectively.

different energy conversion efficiencies according to Fig. 3a. Specifically, the cooling pump of Motor 1 is triggered when Motor 1 temperature reaches the threshold level at 2711 s for the first time. Pump 1 turns on and off for around 60 seconds followed by a continuous working period till it is temporarily turned off in the second inner urban phase as Motor 1 cools down passively due to the light power demand during that phase. Regarding Motor 2, its temperature is below the pump threshold for the majority of the mission, hence Pump 2 is not triggered until 6226 s, before the end of the mission.

Fig. 6 demonstrates the duration of different motor temperatures as percentages of total mission time, for each motor. The temperature of Motor 1 has the largest duration percentage of 43% between 65°C and 75°C, reaching a total duration of 49% when the temperature is above 65°C (pump threshold temperature). On the other hand, the percentage of temperature range between 55°C and 65°C is the highest for Motor 2, taking up 56%, while Motor 2 has less than 1% of time that triggers the cooling Pump 2. Both Figs. 5 and 6 show that, under the control of the proposed OCP-T scheme, the two motors maintain different temperature levels during the mission and there is a significant temperature gap between the two motors.

The temperature difference between the two motors is directly caused by the imbalanced power distribution between the motors. Since the two motors have identical speeds when driving the EB, the power (and hence the temperature) difference between the motors is caused by the torque magnitude difference between the two motors. As illustrated in Fig. 7, the operating points of Motor 1 and Motor 2 are plotted on motor energy efficiency maps at T=50°C (left), T=55°C (middle), and T=65°C (right), which are the approximated average temperatures of the three phases in the UKBC mission, respectively. It shows that Motor 1 provides larger magnitude torques compared with Motor 2 for all three temperature cases. Specifically, Motor 1 operating points are mainly located between 600 Nm and 1500 Nm, meanwhile undertaking the majority of negative braking (regenerating) torques. The operating region of Motor 2 is more concentrated between positive and negative 600 Nm torques during the mission. Especially when motor angular speed is large (above 600 rpm), Motor 1 delivers larger driving torque magnitudes compared with Motor 2, hence contributing the majority of large-magnitude output power and eventually reaching a higher temperature than Motor 2, as shown in Fig. 5.

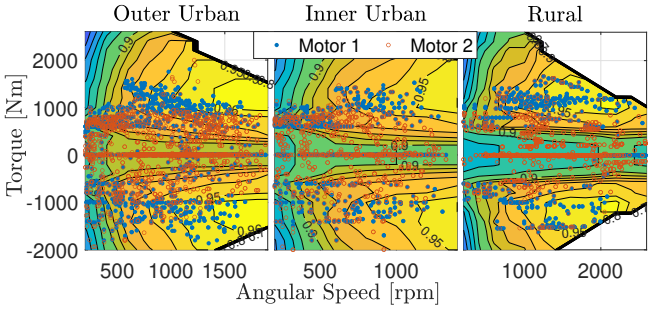

Fig. 7: Operating points of Motor 1 and Motor 2 during outer urban, inner urban, and rural phases of the 2-iteration UKBC mission plotted on energy conversion efficiency maps.

Based on the above performances of the two motors, it can be concluded that under the proposed OCP-T algorithm, Motor 1 and Motor 2 undertake large- and small-magnitude torques, respectively, and hence reach higher and lower motor temperatures, accordingly. Since motor efficiency drops more significantly at smaller-magnitude torque ranges as the temperature increases, the optimal torque split of OCP-T enables the motor that contributes smaller-magnitude torques (i.e., Motor 2) to work at relatively high-efficiency regions to reduce losses during either propulsion or braking.

B. Comparison between OCP-T and benchmark methods

This section compares the energy consumption between the proposed OCP-T method and other benchmark methods including a single-motor powertrain benchmark, two rule-based dual-motor powertrain benchmarks, and another optimization-based benchmark OCP-A. The single-motor powertrain benchmark represents an existing electrification solution that utilizes a single VOITH HD e-motor to drive a three-axle double-deck EB [29]. In the following single-motor powertrain simulations, when the demanded braking power exceeds the limit of a single motor regenerative capability, excess braking is provided by a traditional mechanical brake and therefore the excess braking power is lost. Regarding dual-motor powertrain benchmarks, the two rule-based benchmarks are named equal distribution mode (EDM) and sequential operation mode (SOM). In EDM, the two motors work simultaneously and evenly share the required total power demand. This method ensures the power demand is equally distributed between two motors, avoiding the overuse of one motor. By SOM, only one motor operates at a time, except when the power demand exceeds the limit of a single motor and the second motor works to meet the overall demand. When this limit is not exceeded the first motor works alone until both of the following conditions are met: a) it heats up exceeding the threshold of 65°C (which in any case triggers its associated cooling pump), and b) the temperature of the other motor is below 63°C. Once these conditions are met, the first motor temporarily shuts down to cool off, while the second cooler motor takes over the workload to satisfy the power demand alone. When the second motor satisfies similar conditions as defined above for the first motor, the operation shifts back to the first motor and the procedure repeats. By this alternating sequential operating pattern, each motor operates in succession to maintain the drive cycle while avoiding overheating. The OCP-A benchmark is identical to OCP-T except that it replaces (3) in (8) by

$$P_{e,i}^{25}(k) = \frac{P_{m,i}(k)}{\eta_i(\tau_i(k), \omega(k), 25)^{\text{sign}(\tau_i(k))}}, \tag{9}$$

where the superscript 25 indicates the 25°C temperature of the utilized map. The OCP-A benchmark represents a dual-motor energy management scheme that does not consider thermal effects on energy consumption. For a fair comparison with other methods, following the calculation of the optimal motor torques by OCP-A optimization, the OCP-A scheme evaluates the energy consumption by utilizing the calculated torques in a simulation with the realistic temperature-dependent motor system with efficiency maps shown in Fig. 3a. The dual-motor powertrain is equipped with two VOITH HD e-motors that are identical to the single motor of the single-motor powertrain benchmark.

Table II summarizes the energy consumption calculation method for the various methodologies, which involve either an optimization with temperature independent motor system with the single efficiency map of 25°C shown in Fig. 3a ('Optimization (thermal-unaware)'), or an optimization with temperature-dependent motor system with efficiency maps shown in Fig. 3a ('Optimization (realistic)'), or simulation with temperature-dependent motor system with efficiency maps shown in Fig. 3a ('Simulation (realistic)'), or by an optimization followed by simulation (OCP-A case).

It is shown in Table III that the single-motor powertrain benchmark (denoted as Single) consumes the most energy among all methods as there is only one motor that provides all the demanded driving power; the average motor temperature of the single-motor powertrain is around 86°C, which is much higher (and therefore has worse efficiency) than the average temperature of around 56°C of the two motors in the dual-motor powertrain controlled by the various methods shown in Table III. The rule-based benchmarks EDM and SOM consume 101652 kJ and 100400 kJ of electric energy from the battery, respectively. Furthermore, the OCP-A benchmark draws 97350 kJ net energy from the battery, which is better than the rule-based benchmarks but is still less efficient compared with the temperature-aware method OCP-T that consumes 94250 kJ of battery electric energy and which is the least consuming among all powertrain control methods. More specifically, it can be observed in Table III that OCP-T distributes the consumed and generated energy more equally between the two motors than OCP-A that uses Motor 1 much more than Motor 2. Thus, OCP-T avoids overheating of one motor and hence inefficient operation of that motor, leading to the least total energy consumption. In addition, it is noticeable that the OCP-T method consumes the least amount of energy for operating cooling pumps.

TABLE II: Battery energy consumption calculation method of benchmark and proposed methods.

Calculation Method	Single	EDM	SOM	OCP-A	OCP-T
Optimization (thermal-unaware)				×	
Optimization (realistic)					×
Simulation (realistic)	×	×	×	×	

TABLE III: Energy consumption by different powertrain control methods.

Methods	Energy Consumption (kJ)					
	Net Battery	Motor 1		Motor 2		Total Pumps
		Consumed	Generated	Consumed	Generated	
Single	107052	246916	-140701			837
EDM	101652	123101	-72603	123101	-72603	656
SOM	100400	120180	-73474	122908	-69694	480
OCP-A	97350	203077	-107585	40032	-38801	627
OCP-T	94250	139427	-88907	101619	-58387	498

The net battery energy consumption in Table III is visualized in Fig. 8. Evaluating energy-saving performances by choosing the results of the single-motor powertrain as a normalized baseline, as indicated by the solid line, the dual-motor powertrain can achieve 5.04% and 6.21% energy savings by the rule-based EDM and SOM methods, and a 9.06% energy saving by the OCP-A method, respectively. Moreover, the proposed OCP-T scheme can save 11.96% battery energy consumption. When comparing the battery energy consumption of OCP-T with other dual-motor benchmarks, OCP-T achieves 7.28% and 6.13% reduction compared with rule-based EDM and SOM methods, respectively. These benefits are gained by adopting optimal motor operating points solved by the optimization. Furthermore, OCP-T achieves a 3.18% energy saving compared to the OCP-A benchmark, which is a direct result of considering realistic temperature-dependent efficiency maps in OCP-T. Moreover, Fig. 8 illustrates the composition of battery electric energy consumption in terms of energy consumption in each phase of the 2-iteration UKBC mission for each method. The percentages shown in the breakdown of each powertrain method denote the relative energy consumption of a particular phase in that method with respect to the same phase of the single-motor powertrain method. Overall, approximately half of the consumed energy in each method is used to carry out the Rural phase which is the fastest but also the shortest in time phase. The Inner Urban phase uses the least amount of energy due to its slowest average speed and the shortest traveled distance.

The higher energy consumption on rural as compared to urban routes suggests that the electrification of intercity buses should pay specific attention to both the bus powertrain energy efficiency and the range specification.

To summarize, the presented OCP-T method can significantly save energy consumption by keeping the motors at optimal operating points and considering realistic thermal effects of the motors. Moreover, thanks to the benefit of keeping average motor temperatures at proper levels, this proposed method contributes to improving the motor lifespan, thereby reducing maintenance costs for the bus operator.

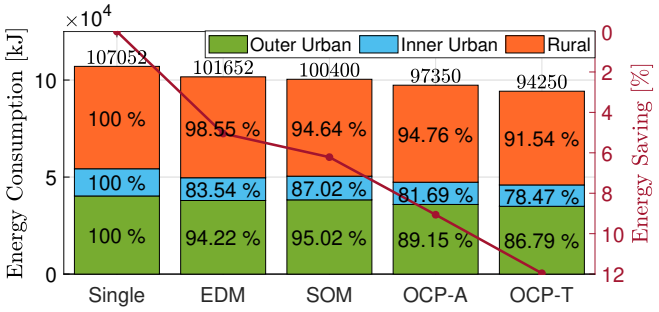

Fig. 8: Overall battery energy consumption breakdown in terms of energy consumption in each of the outer urban, inner urban, and rural phases of the 2-iteration UKBC mission, by OCP-T and other benchmark methods.

V. Conclusion and Future Work

This work addresses the energy management problem of the heavy-duty electric bus equipped with two electric motors. The work begins with collecting experimental data on electric motor temperature, input electric power, and angular speed on an industrial grade motor (VOITH Liquid-cooled IPSM HD e-motor). With the obtained experimental data, a motor temperature dynamic model is identified and fitted by a first-order system model. In addition, motor energy conversion efficiency maps at different motor temperatures are also generated. Based on the fitted model dynamics and temperature-dependent efficiency map, a novel globally optimal motor-temperature-aware dual-motor electric bus energy management scheme accounting for the motor efficiency thermal effects is proposed and evaluated for a realistic bus drive cycle. The performance of the proposed scheme is analyzed and compared with an existing single-motor powertrain benchmark, two rule-based dual-motor benchmarks, and another optimization-based but temperature-unaware benchmark, presenting an overall battery electric energy saving of up to approximately 12%. In future work, modifications of the current framework will be expected to enable the real-time implementation of the scheme.

References

[1] X. Yu, S. LeBlanc, N. Sandhu, L. Wang, M. Wang, and M. Zheng, "Decarbonization potential of future sustainable propulsion—A review of road transportation," *Energy Science & Engineering*, vol. 12, no. 2, pp. 438–455, 2024.

[2] Z. Wang, J. Zhou, and G. Rizzoni, "A review of architectures and control strategies of dual-motor coupling powertrain systems for battery electric vehicles," *Renewable and Sustainable Energy Reviews*, vol. 162, p. 112455, 2022.

[3] X. Hu, Y. Li, C. Lv, and Y. Liu, "Optimal energy management and sizing of a dual motor-driven electric powertrain," *IEEE Transactions on Power Electronics*, vol. 34, no. 8, pp. 7489–7501, 2018.

[4] A. De Keyser, M. Vandeputte, and G. Crevecoeur, "Convex mapping formulations enabling optimal power split and design of the electric drivetrain in all-electric vehicles," *IEEE Transactions on Vehicular Technology*, vol. 66, no. 11, pp. 9702–9711, 2017.

[5] Z. Yang, J. Wang, G. Gao, X. Shi *et al.*, "Research on optimized torque-distribution control method for front/rear axle electric wheel loader," *Mathematical Problems in Engineering*, vol. 2017, 2017.

[6] K. Kwon, M. Seo, and S. Min, "Efficient multi-objective optimization of gear ratios and motor torque distribution for electric vehicles with two-motor and two-speed powertrain system," *Applied Energy*, vol. 259, p. 114190, 2020.

[7] M. Hu, J. Zeng, S. Xu, C. Fu, and D. Qin, "Efficiency study of a dual-motor coupling EV powertrain," *IEEE Transactions on Vehicular Technology*, vol. 64, no. 6, pp. 2252–2260, 2015.

[8] C. Zhang, S. Zhang, G. Han, and H. Liu, "Power management comparison for a dual-motor-propulsion system used in a battery electric bus," *IEEE Transactions on Industrial Electronics*, vol. 64, no. 5, pp. 3873–3882, 2017.

[9] J. Ruan, C. Wu, H. Cui, W. Li, and D. U. Sauer, "Delayed deep deterministic policy gradient-based energy management strategy for overall energy consumption optimization of dual motor electrified powertrain," *IEEE Transactions on Vehicular Technology*, 2023.

[10] Z. Li, A. Khajepour, and J. Song, "A comprehensive review of the key technologies for pure electric vehicles," *Energy*, vol. 182, pp. 824–839, 2019.

[11] H. Cui, J. Ruan, C. Wu, K. Zhang, and T. Li, "Advanced deep deterministic policy gradient based energy management strategy design for dual-motor four-wheel-drive electric vehicle," *Mechanism and Machine Theory*, vol. 179, p. 105119, 2023.

[12] E. Gundabattini, A. Mystkowski, A. Idzkowski, R. S. R., and D. G. Solomon, "Thermal mapping of a high-speed electric motor used for traction applications and analysis of various cooling methods-A review," *Energies*, vol. 14, no. 5, 2021.

[13] Q. Ai, H. Wei, H. Dou, W. Zhao, and Y. Zhang, "Robust rotor temperature estimation of permanent magnet motors for electric vehicles," *IEEE Transactions on Vehicular Technology*, vol. 72, no. 7, pp. 8579–8591, 2023.

[14] W. Li, Z. Cao, and X. Zhang, "Thermal analysis of the solid rotor permanent magnet synchronous motors with air-cooled hybrid ventilation systems," *IEEE Transactions on Industrial Electronics*, vol. 69, no. 2, pp. 1146–1156, 2022.

[15] A. Wahl, C. Wellmann, C. Monissen, and J. Andert, "Active temperature control of electric drivetrains for efficiency increase," *Applied Energy*, vol. 338, p. 120887, 2023.

[16] I. C. Borbujo, P. G. Pereirinha, M. G. Vega, J. A. del Valle, and J. C. Á. Antón, "Heavy duty transport descarbonization: Legislation and standards for hydrogen and battery electric buses and heavy-duty trucks," in *2021 IEEE Vehicle Power and Propulsion Conference (VPPC)*, 2021, pp. 1–6.

[17] S. P. Holland, E. T. Mansur, N. Z. Muller, and A. J. Yates, "The environmental benefits of transportation electrification: Urban buses," *Energy Policy*, vol. 148, p. 111921, 2021.

[18] D. Smith, B. Ozpineci, R. L. Graves, P. T. Jones, J. Lustbader, K. Kelly, K. Walkowicz, A. Birky, G. Payne, C. Sigler, and J. Mosbacher, "Medium- and heavy-duty vehicle electrification: An assessment of technology and knowledge gaps," National Renewable Energy Laboratory–Oak Ridge National Laboratory, United States, Tech. Rep., 2 2020.

[19] G. Papa, M. Santo Zarnik, and V. Vukasinović, "Electric-bus routes in hilly urban areas: Overview and challenges," *Renewable and Sustainable Energy Reviews*, vol. 165, p. 112555, 2022.

[20] A. L. Rodrigues and S. R. Seixas, "Battery-electric buses and their implementation barriers: Analysis and prospects for sustainability," *Sustainable Energy Technologies and Assessments*, vol. 51, p. 101896, 2022.

[21] B. Spiller, N. Lohawala, and E. DeAngeli, "Medium- and heavy-duty vehicle electrification: Challenges, policy solutions, and open research questions," Resource for the Future, Washington DC, Tech. Rep., 2023.

[22] A. Dennis, "The crowd-shifter: Enviro400EV," 2024, https://www.alexander-dennis.com/buses-coaches/enviro400ev/ (accessed: July 31, 2024).

[23] Volvo, "Volvo BZL Electric," 2024, https://www.volvobuses.com/en/city-and-intercity/chassis/volvo-bzl-electric.html (accessed: July 31, 2024).

[24] A. Dennis, "Enviro500EV Charge," 2023, https://www.alexander-dennis.com/buses-coaches/enviro500ev-north-america/ (accessed: July 31, 2024).

[25] Volvo, "Volvo BZR Electric," 2024, https://www.volvobuses.com/en/city-and-intercity/chassis/volvo-bzr-electric.html (accessed: July 31, 2024).

[26] VOITH, "Next stop: E-Mobility - with the new Voith Electrical Drive System," 2024, https://voith.com/corp-en/drives-transmissions/voith-electrical-drive-system.html?204022%5B%5D=0 (accessed: July 31, 2024).

[27] O. Sundstrom and L. Guzzella, "A generic dynamic programming matlab function," in *2009 IEEE Control Applications, (CCA) & Intelligent Control, (ISIC)*, 2009, pp. 1625–1630.

[28] TFL, "Specification for new buses: Attatchments," London Bus Services Limited, London, Tech. Rep., 2020.

[29] A. Dennis, "The global people-mover: Enviro500EV," 2024, https://www.alexander-dennis.com/buses-coaches/enviro500ev/ (accessed: July 31, 2024).